

# Visible quantum plasmons in highly-doped few-layer graphene

Sharmila N. Shirodkar,<sup>\*,†,||</sup> Marios Mattheakis,<sup>†,⊥</sup> Paul Cazeaux,<sup>‡</sup> Prineha  
Narang,<sup>†,#</sup> Marin Soljačić,<sup>¶</sup> and Efthimios Kaxiras<sup>†,§</sup>

<sup>†</sup>*John A. Paulson School of Engineering and Applied Sciences, Harvard University,  
Cambridge, Massachusetts 02138, USA*

<sup>‡</sup>*School of Mathematics, University of Minnesota, Minneapolis, Minnesota 55455, USA*

<sup>¶</sup>*Department of Physics, Massachusetts Institute of Technology, 77 Massachusetts Avenue,  
Cambridge, Massachusetts 02139, USA*

<sup>§</sup>*Department of Physics, Harvard University, Cambridge, Massachusetts 02138, USA*

<sup>||</sup>*Present address: Department of Materials Science and NanoEngineering, Rice University,  
Houston, TX 77005, USA*

<sup>⊥</sup>*Crete Center for Quantum Complexity and Nanotechnology, Department of Physics,  
University of Crete, PO, Box 2208, 71003 Heraklion, Hellas*

<sup>#</sup>*Faculty of Arts and Sciences, Harvard University, Cambridge MA 02138, USA*

E-mail: sns8@rice.edu

## Abstract

Doped graphene can support plasmon modes, but the limited range of doping achieved by gating prevents their frequency from reaching the visible to infrared range. Here we show, through the use of first-principles calculations, that the high levels of doping achieved by lithium intercalation in bilayer and trilayer graphene shift the plasmon frequencies into the visible range. To obtain physically meaningful results, we introduce a correction of the effect of plasmon interaction across the vacuum in a periodic cell by employing transparent boundary conditions in the direction perpendicular to the layers, a significant improvement over the Exact Coulomb cutoff technique employed in earlier works. We describe the features of these quantum plasmons, including the dispersion relation, losses and field localization. Our findings point to a strategy for fine-tuning the plasmon frequencies in graphene and other two dimensional materials.

## Keywords

visible plasmons, bilayer/trilayer graphene, nano-plasmonics, Li intercalation

With fabrication of two dimensional (2D) materials getting ever more efficient, experimenters are rapidly developing new electronic circuits and devices that harness their uncommon functionalities. Plasmonic excitations is a crucial capability of many devices, with possible applications ranging from biosensing,<sup>1-3</sup> to subwavelength optics<sup>4</sup> and non-linear optics,<sup>5,6</sup> to nano-antennas<sup>7</sup> and even to metamaterials.<sup>8,9</sup> Since plasmons in 2D materials can propagate only in the plane of the layer and decay away from it, they achieve ultra subwavelength confinement with phase velocities several orders of magnitude lower than the speed of light.<sup>10</sup> The origin of 2D plasmons is related to the local field effects and the non-local response of the material to external fields,<sup>11</sup> implying that the study of these wave modes demands a fully quantum mechanical description of the material properties. Specifically, the dielectric function is not a simple superposition of the dielectric contributions of its components, as in a classical system, and the classical solution of Maxwell's equations for

the multilayer structures we consider would not resolve the individual layers to identify the multiple plasmon modes associated with them; for these reasons, we refer to 2D plasmons in these structures as ‘quantum’.

A material with intriguing properties in the context of 2D plasmons is graphene.<sup>12</sup> Some of graphene’s special properties in relation to plasmon excitations are its extremely high electrical mobility<sup>13</sup> and the easily tunable, through gating,<sup>13,14</sup> electron and hole doping concentrations. It is easy to tune the 2D plasmon frequency in graphene-based plasmonic devices, because it is proportional to  $n^{1/4}$ ,  $n$  being the doping concentration;<sup>12</sup> typical  $n$  values achieved by gating are  $\sim 10^{11} \text{ cm}^{-2}$ , corresponding to a shift of the Fermi level from the Dirac point by few tens of meV. The heaviest doping achieved,<sup>15</sup> with hole concentration  $n_h > 10^{13} \text{ cm}^{-2}$ , corresponds to a downward shift of the Fermi level by more than  $-0.5 \text{ eV}$ . The 2D plasmons in graphene generated by doping through gating typically have low frequency, in the infrared to THz range, and seldom in the mid- or near-infrared range.<sup>3,15,16</sup> The latter range would be desirable for applications that involve light-matter interaction but requires heavier doping. One can try going beyond graphene to achieve optical plasmons. However, plasmons in transition metal dichalcogenides (TMDC’s), the other interesting family of 2D materials, are expected to appear at THz frequencies.<sup>17,18</sup> A low energy plasmon mode on the Be(0001) surface has been previously observed in the visible range,<sup>19</sup> but this plasmon emerges from a partially occupied quasi-2D state of the Be(0001) surface and may not be interpreted as a true 2D plasmon, since it will have a finite penetration depth into the underlying bulk material.

Alternatively, one can attempt to dope graphene to levels beyond what is feasible through gating by using other methods. For example, inserting metal atoms like Li between layers of 2D materials is experimentally feasible<sup>20,21</sup> and can lead to heavy doping. Inspired by these facts, we used a theoretical approach based on first-principles electronic structure calculations to explore the possibility of observing quantum plasmons in the visible range for Li-intercalated few-layer graphene. We show that this effect is indeed possible, opening up

pathways for fine-tuning the frequency range of plasmons (especially into the visible range) in 2D structures, which can be accomplished by varying the concentration and type of intercalants. The plasmon frequencies and losses discussed below represent results of high accuracy, obtained through the use of standard first-principles electronic structure methods, enhanced by two key ingredients: the realistic estimation of carrier lifetimes and the imposition of proper boundary conditions in the super-cell of the electronic structure calculations to determine the correct plasmon modes. We describe these key ingredients next.

Our first-principles calculations are based on density functional theory (DFT) as implemented in the GPAW package.<sup>22,23</sup> The interaction between ionic cores and valence electrons is described by the projector augmented wave method.<sup>24,25</sup> To eliminate the interaction between the periodic images, a vacuum of 25 Å is included along the direction perpendicular to the plane of the sheets ( $c$  direction). We use a plane wave basis for the representation of the Kohn-Sham wavefunctions with an energy cutoff of 340 eV, and the Local Density Approximated (LDA) functional for the exchange-correlation energy of the electrons. For the linear response calculations, used to estimate the dielectric functions,<sup>26</sup> we sample the Brillouin zone with a  $256 \times 256 \times 1$  grid of  $k$ -points to include an accurate description of intraband transitions. For the dielectric response calculations we use a plane wave energy cutoff of 30 eV and a broadening  $\eta \approx 0.1$  eV. All the other parameters were converged to within 0.05 eV of the plasmon energies, using the methodology developed by Andersen *et al.*<sup>17,27</sup> for calculating the quantum plasmon modes.

Obtaining the plasmon modes relies on the calculation of the linear dielectric response function of the system within the GPAW<sup>26</sup> code, but we use our own method for extracting the plasmon frequency, identified as the value at which real part of dielectric function vanishes, and the corresponding eigenvectors. The potential  $\phi(\mathbf{r}, \omega)$  and charge density  $\rho(\mathbf{r}, \omega)$  of quantum plasmon modes are obtained as left and right eigenfunctions (which satisfy the

Poisson equation) of the dielectric operator  $\hat{\epsilon}(\omega)$ , diagonalized in the plane wave basis:

$$\hat{\epsilon}(\omega)\phi_n(\omega) = [\hat{1} - \hat{v} \hat{\chi}^0(\omega)]\phi_n(\omega) = \lambda_n(\omega)\phi_n(\omega) \quad (1)$$

with the dielectric operator  $\hat{\epsilon}(\omega)$  expressed in terms of the noninteracting linear response operator  $\hat{\chi}^0(\omega)$  and the Coulomb interaction operator  $\hat{v} = 1/|\mathbf{r} - \mathbf{r}'|$ . The condition for observing a plasmon at frequency  $\omega_p$  is that the real part of the dielectric function,  $\text{Re}[\lambda_n(\omega)]$ , goes to 0 from a negative value; this value corresponds to a peak in the loss function,  $-\text{Im}[\lambda_n(\omega)]/|\lambda_n(\omega)|^2$ . When, due to coupling between the interband transitions, the zero in the real part and the peak in the imaginary part do not coincide in frequency,<sup>27</sup> we use the peak in the loss function to identify the plasmon frequency ( $\omega_p$ ).

A key ingredient in obtaining the plasmon dispersion and losses is the carrier lifetime,  $\tau$ . To obtain reliable values of  $\tau$ , we use the DFT results for the energies and matrix elements of both the electrons and the phonons. This takes into account the detailed electronic structure effects such as inter-layer interactions and response of electrons far from the Dirac point, as well as scattering against both acoustic and optical phonons including Umklapp and inter-valley processes.<sup>28,29</sup> This methodology has previously been used to determine the hot carrier generation and relaxation mechanisms in plasmonic metals and the identification of their signatures in ultrafast pump-probe measurements.<sup>30,31</sup> Changing the Fermi level  $E_F$ , changes the equilibrium electron occupation factors in the Boltzmann equation as well as in the Fermi Golden rule; we account for this by explicitly evaluating these quantities for several different values of  $E_F$  ranging from the neutral (undoped) value to 1.5 eV above it. Interestingly, our results show that the extremely large  $\tau \sim 1$  ps for undoped graphene in air drops to  $\sim 29$  fs in doped graphene (see Supplementary information for details).

In the course of calculating plasmon properties, we found that the standard approach for eliminating spurious effects due to finite size of the vacuum region, that is, the 2D Coulomb cutoff applied in the calculation of dielectric function,<sup>32</sup> leads to significant inaccuracies from

the interaction between plasmon modes across the vacuum for small values of in-plane plasmon wave-vectors ( $\mathbf{q}$ ). Increasing the size of the vacuum region until these effects become negligibly small requires very expensive calculations. A significant methodological contribution of the present work is the formulation and implementation of transparent boundary conditions which overcome the drawbacks of the Coulomb cutoff method and offer a more accurate description of the quantum plasmon fields. In the DFT calculation, a rectangular cell is used with periodic boundary conditions in all three directions. In the random phase approximation (RPA), the linear response operator is obtained in reciprocal space as a matrix  $\chi_{\mathbf{G},\mathbf{G}'}^0(\mathbf{q},\omega)$ , where  $\mathbf{G}$  and  $\mathbf{G}'$  are vectors belonging to the reciprocal lattice,  $\mathbf{q}$  is the plasmonic in-plane wave vector, and  $\omega$  is the frequency. We assume periodicity only in the  $(x,y)$  plane for the purpose of solving equation (1) to determine the quantum plasmon modes. Let  $z_-, z_+$  be the bounds of the simulation box along the  $z$  direction. We apply a one-dimensional Fourier transform in the  $z$  direction to obtain a real space representation in this coordinate. The response operator then has the form:

$$\hat{\chi}^0\phi(z, \mathbf{G}_{xy}, \mathbf{q}, \omega) = \int_{z_-}^{z_+} \sum_{\mathbf{G}'_{xy}} \chi_{\mathbf{G}_{xy}, \mathbf{G}'_{xy}}^0(z, z', \mathbf{q}, \omega) \phi(z', \mathbf{G}'_{xy}, \mathbf{q}, \omega) dz', \quad (2)$$

where  $\mathbf{G}_{xy}, \mathbf{G}'_{xy}$  are vectors of the in-plane reciprocal lattice. For values of  $z, z'$  inside the simulation cell,  $z_- < z, z' < z_+$ , the kernel  $\chi_{\mathbf{G}_{xy}, \mathbf{G}'_{xy}}^0(z, z')$  is deduced from  $\chi_{\mathbf{G}, \mathbf{G}'}^0$  by Fourier transform. The kernel is extended with zero values for  $z$  or  $z'$  that lie in the vacuum region outside of this cell. We observe next that equation (1) can be reformulated as the generalized eigenvalue problem (see Supplementary information for details):

$$\hat{\chi}^0\phi_n(z, \mathbf{G}_{xy}, \mathbf{q}, \omega) = \frac{1 - \lambda_n}{4\pi} \left( |\mathbf{q} + \mathbf{G}_{xy}|^2 - \frac{\partial^2}{\partial z^2} \right) \phi_n(z, \mathbf{G}_{xy}, \mathbf{q}, \omega), \quad (3)$$

with the additional constraint that  $|\phi_n| \rightarrow 0$  as  $z \rightarrow \pm\infty$  so the problem is well-posed. Since the left-hand side vanishes in the vacuum region, equation (3) reduces to the one-dimensional

Poisson equation. For any nonzero value of  $|\mathbf{q} + \mathbf{G}_{xy}|$ , we thus obtain an explicit solution

$$\phi_n(z, \mathbf{G}_{xy}, \mathbf{q}, \omega) = \phi_n(z_{\pm}, \mathbf{G}_{xy}, \mathbf{q}, \omega) e^{-|\mathbf{q} + \mathbf{G}_{xy}| |z_{\pm} - z|} \quad \text{for } z \leq z_- \text{ and } z \geq z_+.$$

The continuity of  $\phi_n$  and its first derivative with respect to  $z$  lead to the transparent boundary conditions at  $z = z_{\pm}$ :

$$\frac{\partial \phi_n}{\partial z}(\mathbf{q}, \mathbf{G}_{xy}, z_{\pm}, \omega) = \mp |\mathbf{q} + \mathbf{G}_{xy}| \phi_n(\mathbf{q}, \mathbf{G}_{xy}, z_{\pm}, \omega) \quad (4)$$

which implies that the charge density and potential do not see the periodic boundary along the  $z$  direction for any value of  $\mathbf{q}$ , and hence decay to zero as  $z \rightarrow \pm\infty$ . We solve numerically by finite differences the eigenvalue problem of equation (3) restricted to the finite band  $z_- \leq z \leq z_+$ , with the boundary conditions equation (4).

While the notion of achieving high levels of doping through controlled intercalation can be applied to various few-layer systems, we choose bilayer and trilayer graphene intercalated with Li as the prototypical 2D systems to demonstrate the emergence of quantum plasmons in the visible range of frequencies. We model the multilayers with an in-plane  $\sqrt{3} \times \sqrt{3}$  multiple of the primitive unit cell of graphene, with the graphene/lithium/graphene (G/Li/G) and graphene/lithium/graphene/lithium/graphene (G/Li/G/Li/G) systems in the AA stacking configuration; there is 1 Li atom per unit cell between each pair of layers (see Fig. 1).<sup>33,34</sup> For the trilayer, we consider the structure with the two Li atoms at the same hollow site but between two different pairs of layers, since the most stable configuration is the one with no relative shift between the Li layers.<sup>34</sup> After Li intercalation, the separation between the layers increases by 0.14 Å and by 0.11 Å relative to its value in the AA stacked graphene bilayer (3.52 Å), for the bilayer and trilayer, respectively. Intercalation also leads to charge transfer from Li to the graphene layers, and renders the system metallic (see Fig. 1). The amount of charge transferred depends on the electronic structure of the individual layer and determines the stability of the intercalated system.<sup>33</sup> Since graphene is a zero band gap

material, it readily accepts charge and remains energetically stable at the Li intercalation concentrations studied here. Using Bader analysis to calculate the charges, we find that the amount of charge transferred from Li to the layers is approximately  $0.84 e$  and  $0.87 e$  for the bilayer and the trilayer. The structures have inversion symmetry due to the AA stacking of the graphene layers and the symmetry of the intercalated Li atoms, and the plasmon modes reflect this symmetry.

In the absence of Li intercalation, the Fermi level is at the Dirac point for the G/G and G/G/G structures. The high symmetry K point in the Brillouin Zone (BZ) of the primitive cell, where the Dirac point of the monolayer appears, folds onto the  $\Gamma$  point in the BZ of the  $\sqrt{3} \times \sqrt{3}$  unit cell in our simulations. Hence, the Dirac cones of the AA stacked graphene layers appear at the  $\Gamma$  point in the band structure plots (see Fig. 1). The AA stacking of the graphene layers preserves the sublattice symmetry of both layers and the linear dispersion of the electron bands at the Dirac point, unlike in the AB stacking where the bands are parabolic. Since the material is metallic due to the presence of finite number of states at the Fermi level on account of the AA stacking, plasmons due to both intraband<sup>35,36</sup> and interband transitions can be observed. The interband transitions are overdamped for low doping levels, implying that the plasmons decay through interband losses. For graphene, these high frequency plasmons damped by interband losses appear at  $\sim 5$  eV, known as “ $\pi$ ”plasmon, and 14 eV known as “ $\pi + \sigma$ ”plasmon,<sup>37,38</sup> but there exist no reports of undamped intra/interband plasmons in the visible range of frequencies.

Since we consider multiple layers, more than one plasmon modes emerge.<sup>17,27,39</sup> The modes can be differentiated on the basis of the phase of the potential and charge density fields of the plasmon in the layers, as symmetric or antisymmetric [see Fig. 2(a)] in a bilayer system. In trilayer graphene the charge density of the symmetric mode is in phase and the antisymmetric mode is out of phase at the outermost layers, Fig. 2(d). The tail of the 2D plasmon in graphene extends to  $\sim \lambda_p/2\pi$ ,  $\lambda_p$  being the plasmon wavelength. This means that at small in-plane plasmon wave-vectors, the tail extends beyond the vacuum region in

the simulations. For example, a 2D plasmon of 20 nm wavelength simulated in a cell with 25 Å vacuum, having a tail of  $\sim 30$  Å, would interact with its periodic images and give rise to spurious fields and pseudo charges at the vacuum boundaries. These spurious fields are corrected by our transparent boundary conditions, wherein the plasmon field decays to zero at infinity, making the the periodic images of the plasmon tails invisible to one another (see Methods). The transparent boundary conditions allow us to investigate the properties of long wavelength plasmons without having to increase the size of the vacuum region. This is shown explicitly in Fig. 2(a) and (d) for the G/Li/G and G/Li/G/Li/G systems, where we compare the charge density of the quantum plasmon modes with and without the use of transparent boundary conditions, the latter employing the Coulomb cutoff method,<sup>32</sup> in which case the interaction between periodic images across the vacuum produces a non-decaying potential field and pseudo charges at the boundary.

Intercalating the graphene bilayer with Li leads to n-doping and moves the Fermi level from the Dirac point into the conduction band by 1.35 eV, as shown in Fig. 1(a), which corresponds to a doping concentration of  $5 \times 10^{14}$  cm<sup>-2</sup> for composition LiC<sub>12</sub>. The charge transferred from Li (0.84  $e$  per unit cell) is equally distributed in the unoccupied  $\pi^*$  orbitals of both the layers. The consequences of charge transfer are evident in the charge density fields of the plasmon modes, Fig. 2(a), where the intensity of the fields is equal and reaches the maximum/minimum values away from the layers, consistent with the fact that the  $\pi^*$  orbitals of graphene extend away from the layers.

We plot the plasmon dispersion along  $\Gamma$  to M (the  $\Gamma$  to K direction is not as interesting in the band structure) by carrying out the same analysis for a range of in-plane wave-vectors, with the magnitude of the real part of  $\mathbf{q}$  between  $|\mathbf{q}| = q = 0.007$  Å<sup>-1</sup> and  $0.21$  Å<sup>-1</sup>. Both plasmon modes become very weak above  $q = 0.21$  Å<sup>-1</sup> but the symmetric mode exhibits higher variation in the peak frequency and height as compared with the antisymmetric mode, implying that the symmetric mode is more dispersive. The antisymmetric mode has a higher spectral weight in agreement with previous reports.<sup>15,39</sup> From the plasmon dispersion,

Fig. 2(b), we find that the symmetric mode varies as  $\sqrt{q}$  at small magnitudes of  $\mathbf{q}$  which corresponds to the classical plasmon with Drude behavior due to intraband transitions, whereas the antisymmetric mode varies almost linearly with  $q$  (and has finite frequency at  $q=0$ ) and is related to the higher interband transitions between the perfectly nested bands of the two layers.<sup>39</sup> In bilayer graphene the plasmon frequencies are between 0.8 eV to 2.2 eV for  $q \geq 0.007 \text{ \AA}^{-1}$ , the antisymmetric mode is in the optical frequency range even at low  $q$ , whereas the symmetric mode enters into this range at higher  $q$  values. The symmetric mode is always lower in energy than the antisymmetric mode due to finite coupling.<sup>39</sup>

A concrete measure of the plasmon losses is the ratio of the real to the imaginary component of the plasmon wave-vector  $\mathbf{q}$ ,  $\text{Re}[q]/\text{Im}[q]$ , shown in Fig. 2(c), which corresponds to the number of plasmon wavelengths that propagate before it loses most of its energy. We have calculated the value of  $\text{Im}[q]$  under the Random Phase Approximation using the formalism developed by Jablan *et al.*<sup>36</sup> The value of  $\tau$ , which is a function of doping concentration, including electron-electron and electron-phonon scattering is  $\sim 29$  fs when the Fermi level shifts by 1.35 eV in graphene. We note that  $\tau$  is 135 fs<sup>36</sup> for the Fermi level at 0.135 eV. We only give the ratio for the symmetric (intraband) mode in Fig. 2(c). Since the antisymmetric mode has a linear dispersion, its frequency range is narrow compared to the symmetric mode, and hence the variation of the  $\text{Re}[q]/\text{Im}[q]$  is not as pronounced as that of the symmetric mode (refer to Supplementary Fig. S1 for further details). The in-plane propagation length of the plasmons varies directly with this ratio, with the symmetric plasmons propagating longer at longer wavelengths ( $\lambda_{air}$ ). We also calculate the wave “shrinkage” or the field localization of the plasmons, shown in Fig. 2(c); this corresponds to the ratio by which the plasmon wavelength is smaller than that in vacuum, and is approximately 100 times for bilayer graphene. There are three important decay modes that lead to plasmon damping: Landau damping due to intraband losses when  $\omega < \omega_{intra}$ , interband losses where the interband transitions (single particle excitations, SPE) result in formation of electron hole pairs for  $\omega > \omega_{SPE}$ , and decay via optical phonons in graphene for  $\omega > \omega_{ph}$  ( $\omega_{ph} = 0.2$

eV or  $6.2 \mu\text{m}$ ).<sup>36</sup> The highest frequency optical phonon with maximum coupling with electrons in Li intercalated graphene is  $\omega_{ph} = 1400 \text{ cm}^{-1} \equiv 0.17 \text{ eV}$ .<sup>34,40</sup> Since the range of the symmetric and antisymmetric modes (0.8 eV to 2.2 eV) is well above  $\omega_{ph}$  for  $q \geq 0.007 \text{ \AA}^{-1}$ , only multiple scatterings by phonons (which are less likely) will scatter plasmons into Landau damping regions. On the other hand, plasmons with high frequencies within range  $\omega_{SPE} - \omega_{ph}$  to  $\omega_{SPE}$  can get scattered by phonons into Landau damped regions. Hence, interband transitions and optical phonons damp plasmons for  $\omega > \omega_{SPE} - \omega_{ph}$ , leaving lower frequency modes undamped.

The regions damped by single particle excitations are defined by the poles of the response function,<sup>39,41</sup> and correspond to the interband continuum. The poles of the response function at  $q=0$  were identified at 0 eV, 0.6 eV and 2.4 eV originating from the intraband, low energy interband and the electron-hole interband transitions in the Li intercalated AA stacked bilayer graphene. The damping regions are defined by  $E_{SPE} \pm \hbar v_F q \pm \omega_{ph}$  (including scattering by optical phonons), where  $v_F$  is the Fermi velocity and  $E_{SPE}$  is the single particle excitation energy<sup>35,41</sup> (see gray shaded areas in Fig. 2(b)). We confirmed that the area in the damping regime is proportional to the width of the imaginary component of the response function, which validates our results. Heavy doping by lithium pushes the electron-hole interband threshold for the bilayer to  $\omega_{inter} \approx 1.77 \text{ eV}$  ( $\lambda = 0.7 \mu\text{m}$ ). Since the optical frequency range ( $\omega_{op}$ ) is between 1.59 eV to 3.26 eV ( $\lambda = 0.38 \mu\text{m}$  to  $0.78 \mu\text{m}$ ) and  $\omega_{inter} < \omega_{op}$ , most of the symmetric and antisymmetric plasmon modes in this range are not damped by the interband transitions, which involves the formation of electron-hole pairs indicated by the shaded regions in Fig. 2(b) and 2(e). Only for  $q \geq 0.06 \text{ \AA}^{-1}$  are the symmetric and antisymmetric modes damped. The symmetric intraband mode has finite  $\text{Re}[q]/\text{Im}[q]$  (by extrapolation) in the mid-infrared region ( $3 \mu\text{m} < \lambda_{air} < 50 \mu\text{m}$ ).<sup>15</sup>

To push the interband threshold frequency, and hence the plasmon frequencies, higher into the optical range ( $> 2 \text{ eV}$ ), the Fermi level needs to be moved farther into the conduction bands. Since the maximum possible intercalation in bilayer graphene corresponds to com-

position  $C_{12}Li$ , additional Li can be incorporated only by having more than two graphene layers. We therefore explore trilayer graphene since it can accommodate two Li layers, with a composition  $Li_2C_{18}$ , and increases the doping level. In trilayer graphene the higher concentration of Li shifts the Fermi level higher into the conduction band, by 1.51 eV relative to the Dirac point, as shown in Fig. 1(b) with corresponding doping concentration of  $1 \times 10^{15} \text{ cm}^{-2}$  and 0.87  $e$  per unit cell charge transferred from Li to the graphene layers.

There are three modes in the trilayer structure in the frequency range 1.2 – 2.8 eV along the  $\Gamma$  to M direction for  $q \geq 0.007 \text{ \AA}^{-1}$ , two of which are symmetric and one antisymmetric, shown in Fig. 2(d). The third graphene layer brings in additional nesting of the bands and leads to the emergence of the third mode (second symmetric) mode. Similar to the bilayer case, the first symmetric mode due to intraband excitations exhibits  $\sqrt{q}$  dependence and the other two modes disperse linearly, see Fig. 2(e). The loss function shows larger variations in the peak positions for the first symmetric mode due to  $\sqrt{q}$  behavior at low  $q$  as compared to the antisymmetric mode (see Supplementary Fig. S2 for details). More interestingly, the first symmetric and antisymmetric bands in the dispersion spectrum (red and blue curves in Fig. 2(e)) intersect and the symmetric and antisymmetric modes are degenerate for  $q > 0.067 \text{ \AA}^{-1}$  along the  $\Gamma$  to M direction. The reason behind this unusual degeneracy is the fine nesting between the bands and consequently the absence of coupling between the two modes.<sup>39</sup>

As expected, the higher doping concentration pushes the interband threshold frequency ( $\omega_{inter}$ ) to  $\approx 2.0 \text{ eV}$  ( $0.62 \text{ \mu m}$ ) for the first symmetric and antisymmetric modes in trilayer Li intercalated graphene. The poles at 0 eV, 0.64 eV, 0.93 eV and 2.5 eV correspond to the three damping regions associated with intraband, low energy interband, and higher energy electron-hole interband transitions. Hence, for  $1.59 \text{ eV} < \omega < 2.0 \text{ eV}$  ( $0.62 \text{ \mu m} < \lambda_{air} < 0.78 \text{ \mu m}$ ) the first symmetric and antisymmetric modes are undamped. More importantly, the second symmetric mode gets damped at a higher frequency, that is, for  $\omega > 2.2 \text{ eV}$ , so all three plasmon modes are undamped and emerge in the optical range for  $q < 0.05 \text{ \AA}^{-1}$ . The  $\tau$  for such high doping concentrations is small  $\approx 19 \text{ fs}$  when the Fermi level shifts by

1.51 eV in graphene. From the ratio of the real and imaginary components of  $\mathbf{q}$ , Fig. 2(f), we find that the first symmetric mode can be observed further into the mid-infrared range (from extrapolation) ( $\lambda_{air} > 3 \mu\text{m}$ ), whereas the other two modes have shorter wavelengths ( $\lambda_{air} < 0.62 \mu\text{m}$ ). The plasmon wavelength is also shrunk by approximately 100 times, Fig. 2(f), as in the case for bilayer graphene in agreement with previous reports.<sup>36</sup> We only plot the ratio for the first symmetric (intraband) mode in Fig. 2(f). Since the antisymmetric and second symmetric modes disperse linearly, the variation in the  $\text{Re}[q]/\text{Im}[q]$  is small. These plasmons exhibit similar “shrinkage” as that of the symmetric mode (refer to Supplementary Fig. S2 for further details).

Controlling the number of layers and the concentration of intercalated Li atoms appears to be a feasible method for engineering the properties of visible plasmons for applications. For example, the mid-infrared region plasmons in both the bilayer and trilayer Li-intercalated structures, can be used for plasmonic biosensing.<sup>3,15</sup> We caution that certain technical aspects of the calculations reported here, like the choice of exchange correlation functional for the electronic structure, can affect the electronic spectrum and can shift the plasmon energies to slightly different values than what we reported; such shifts could change the precise values of the damped plasmon frequencies but we do not expect them to alter the overall picture. Damping due to the presence of defects and substrate phonons, features that were not included in the model of the physical system considered here, can also influence the existence of undamped 2D plasmons in the visible frequency range. A detailed analysis of these parameters will constitute the future scope of this work. Our work can be easily extended to explore other multilayers of other 2D materials (such as black phosphorus, transition metal dichalcogenides) with different dopants and/or intercalants (K, Mg, Na etc), opening up new pathways for fine tuning the plasmon dispersion either by varying the number and type of layers, and/or by varying the concentration and type of intercalant atoms.

## Figures

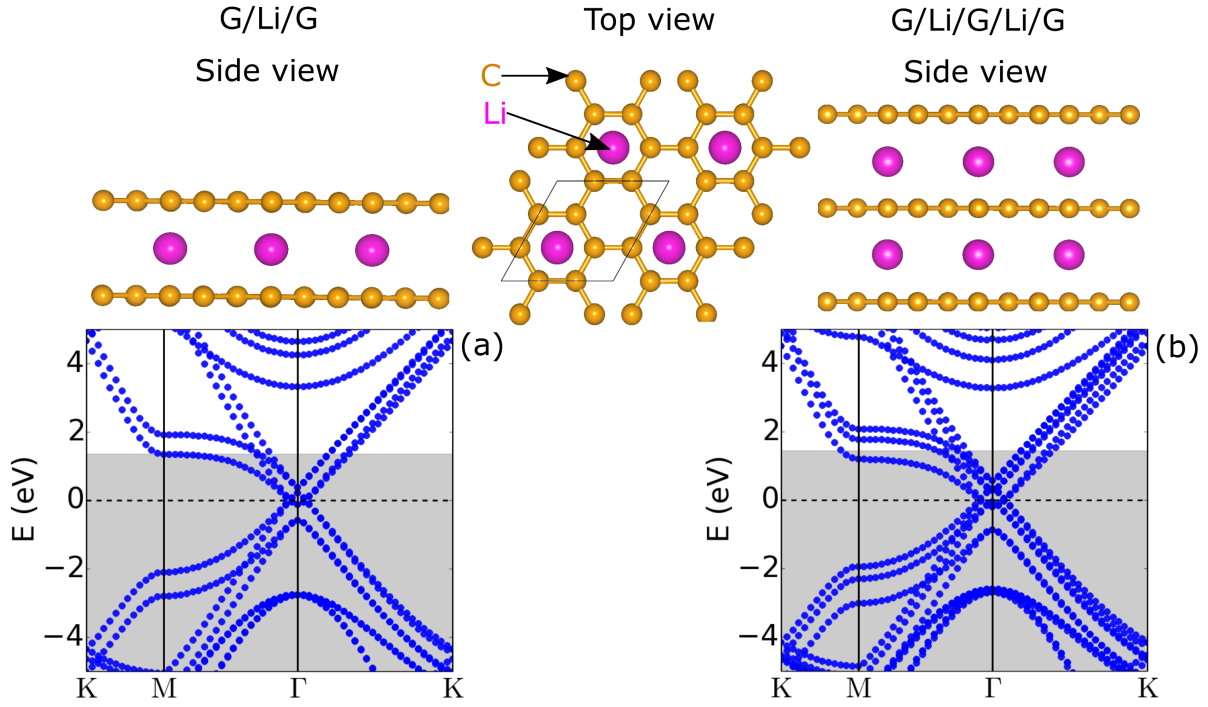


Figure 1: Atomic structures (side and top views) and electronic structures of: (a) the bilayer Li-intercalated graphene (G/Li/G, left) and (b) the trilayer Li-intercalated graphene (G/Li/G/Li/G, right). The shaded regions in (a) and (b) denote the occupied states, and the dashed black lines the Dirac point / Fermi level in undoped layers.

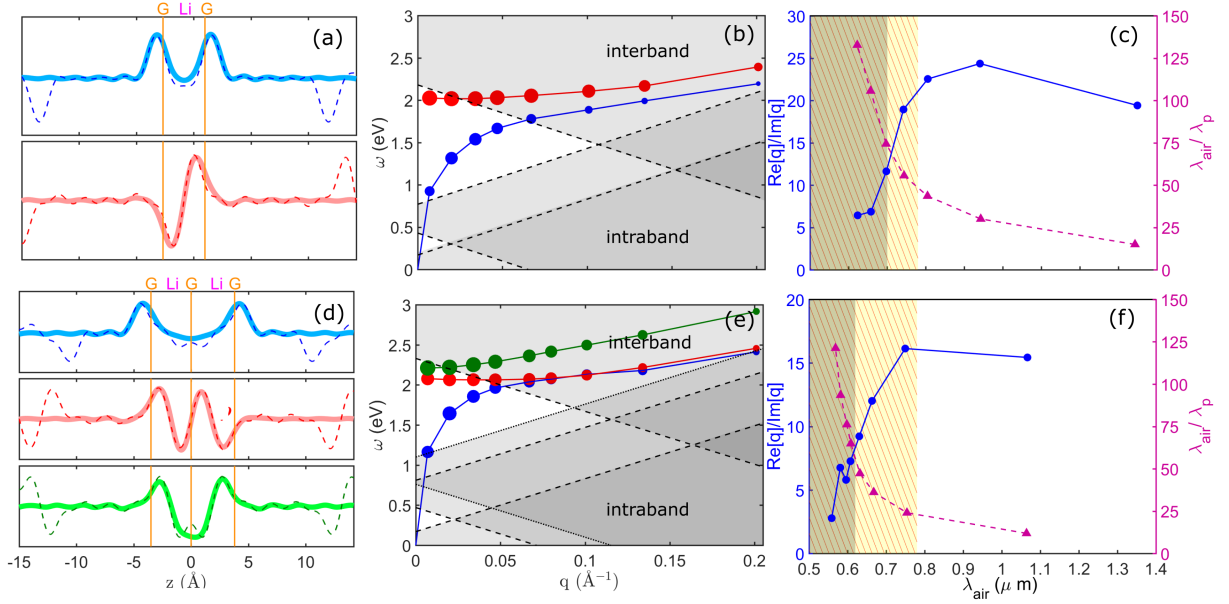


Figure 2: Plasmon features for: (a)-(c), the G/Li/G system, and (d)-(f), the G/Li/G/Li/G system. (a) and (d) Plasmon charge density  $\rho(\mathbf{r})$  at  $q=0.007 \text{ \AA}^{-1}$  for the symmetric modes (blue and green lines) and the antisymmetric mode (red lines); solid lines (thicker and lighter shade) are for results with transparent boundary conditions, dashed lines (thinner and darker shade) for periodic boundary conditions with Coulomb cutoff (see text). (b) and (e) Dispersion relation of plasmons along the  $\Gamma$  to M direction; the diameter of the circles is proportional to the strength of the resonance.<sup>17</sup> Shaded areas represent regions of inter- and intra-band losses (including damping by optical phonon). (c) and (f)  $\text{Re}[q]/\text{Im}[q]$  (left axis, solid line in blue), and field localization (right axis, dashed line in magenta), or “shrinkage”, of the lowest symmetric mode.  $\tau$  is  $\approx 29$  fs and 19 fs for the G/Li/G and the G/Li/G/Li/G systems, respectively. The grey shaded areas denote the region of inter-band losses, and the yellow shaded (hatched) areas denote the visible frequency range, calculated with the Fermi velocity of graphene.

## Author information

### Corresponding Author

\*E-mail: sns8@rice.edu

### Notes

The authors declare no competing financial interest.

## Acknowledgement

The authors thank R. Sundararaman and J. Joannopoulous for ab-initio calculations and discussions related to plasmon lifetimes. The authors also thank J. Cheng, S. Inampudi, H. Mosallaei and G. A. Tritsarlis for useful discussions. MM acknowledges support from EU program FP7-REGPOT-2012-2013-1 under grant agreement 316165 and H2020-MSCA-RISE-2015-691209-NHQWAVE. We acknowledge support by ARO MURI Award No. W911NF14-0247 (SNS and EK) and by EFRI 2-DARE NSF Grant 1542807 (MM). PN and MS were partly supported by the Army Research Office through the Institute for Soldier Nanotechnologies under contract no. W911NF-13-D-0001. We used computational resources on the odyssey cluster of the Research Computing Group at Harvard University, and at the Extreme Science and Engineering Discovery Environment (XSEDE), which is supported by NSF Grant No. ACI-1053575.

## Supporting Information Available

The following files are available free of charge.

The Supporting Information is available free of charge on the ACS Publications website at DOI: xxxxxx/acs.nanolett.xxxxxx The following files are available free of charge.

- supplementary.pdf, loss functions,  $\text{Re}[q]/\text{Im}[q]$  and field localization for symmetric and antisymmetric modes of G/Li/G system and G/Li/G/Li/G systems.

## References

- (1) Bender, F.; Roach, P.; Tsortos, A.; Papadakis, G.; Newton, M. I.; McHale, G.; Gizeli, E. *Measurement Science and Technology* **2009**, *20*, 124011.
- (2) Friedt, J.-M.; Francis, L.; Reekmans, G.; De Palma, R.; Campitelli, A.; Sleytr, U. B. *Journal of Applied Physics* **2004**, *95*.
- (3) Rodrigo, D.; Limaj, O.; Janner, D.; Etezadi, D.; de Abajo, F. J. G.; Pruneri, V.; Altug, H. *Science* **2015**, *349*, 165–168.
- (4) Rivera, V.; Marega Jr, E.; Ferri, F.; Sobreira, F.; Silva, O. *Light transmission via subwavelength apertures in metallic thin films*; Citeseer, 2012.
- (5) Bliokh, K. Y.; Desyatnikov, A. S. *Phys. Rev. A* **2009**, *79*, 011807.
- (6) Davoyan, A. R.; Shadrivov, I. V.; Kivshar, Y. S. *Opt. Express* **2009**, *17*, 21732–21737.
- (7) Dregely, D.; Taubert, R.; Dorfmueller, J.; Vogelgesang, R.; Kern, K.; Giessen, H. *Nat Commun* **2011**, *2*, 267.
- (8) Liu, D.; Guo, Y.; Fang, L.; Robertson, J. *Applied Physics Letters* **2013**, *103*.
- (9) Mattheakis, M.; Valagiannopoulos, C. A.; Kaxiras, E. *Phys. Rev. B* **2016**, *94*, 201404.
- (10) Address, W. F.; Yoon, H.; Yeung, K. Y. M.; Qin, L.; West, K.; Pfeiffer, L.; Ham, D. *Nano Letters* **2012**, *12*, 2272–2277, PMID: 22494364.
- (11) Raza, S.; Toscano, G.; Jauho, A.-P.; Wubs, M.; Mortensen, N. A. *Physical Review B* **2011**, *84*, 121412.
- (12) Fei, Z.; Rodin, A. S.; Andreev, G. O.; Bao, W.; McLeod, A. S.; Wagner, M.; Zhang, L. M.; Zhao, Z.; Thiemens, M.; Dominguez, G.; Fogler, M. M.; Neto, A. H. C.; Lau, C. N.; Keilmann, F.; Basov, D. N. *Nature* **2012**, *487*, 82–85.

- (13) Novoselov, K. S.; Geim, A. K.; Morozov, S. V.; Jiang, D.; Zhang, Y.; Dubonos, S. V.; Grigorieva, I. V.; Firsov, A. A. *science* **2004**, *306*, 666–669.
- (14) Das, A.; Pisana, S.; Chakraborty, B.; Piscanec, S.; Saha, S.; Waghmare, U.; Novoselov, K.; Krishnamurthy, H.; Geim, A.; Ferrari, A.; Sood, A. *Nature nanotechnology* **2008**, *3*, 210–215.
- (15) Yan, H.; Low, T.; Zhu, W.; Wu, Y.; Freitag, M.; Li, X.; Guinea, F.; Avouris, P.; Xia, F. *Nature Photonics* **2013**, *7*, 394–399.
- (16) Grigorenko, A. N.; Polini, M.; Novoselov, K. S. *Nat Photon* **2012**, *6*, 749–758.
- (17) Andersen, K.; Thygesen, K. S. *Phys. Rev. B* **2013**, *88*, 155128.
- (18) Andersen, K.; Latini, S.; Thygesen, K. S. *Nano Letters* **2015**, *15*, 4616–4621, PMID: 26047386.
- (19) Diaconescu, B.; Pohl, K.; Vattuone, L.; Savio, L.; Hofmann, P.; Silkin, V. M.; Pitarke, J. M.; Chulkov, E. V.; Echenique, P. M.; Farias, D.; Rocca, M. *Nature* **2007**, *448*, 57–59.
- (20) Guo, Y.; Smith, R. B.; Yu, Z.; Efetov, D. K.; Wang, J.; Kim, P.; Bazant, M. Z.; Brus, L. E. *The Journal of Physical Chemistry Letters* **2016**, *7*, 2151–2156, PMID: 27203128.
- (21) Sugawara, K.; Kanetani, K.; Sato, T.; Takahashi, T. *AIP Advances* **2011**, *1*.
- (22) Mortensen, J. J.; Hansen, L. B.; Jacobsen, K. W. *Phys. Rev. B* **2005**, *71*, 035109.
- (23) Enkovaara, J. et al. *Journal of Physics: Condensed Matter* **2010**, *22*, 253202.
- (24) Blöchl, P. E. *Phys. Rev. B* **1994**, *50*, 17953–17979.
- (25) Kresse, G.; Joubert, D. *Phys. Rev. B* **1999**, *59*, 1758–1775.

- (26) Yan, J.; Mortensen, J. J.; Jacobsen, K. W.; Thygesen, K. S. *Phys. Rev. B* **2011**, *83*, 245122.
- (27) Andersen, K.; Jacobsen, K. W.; Thygesen, K. S. *Phys. Rev. B* **2012**, *86*, 245129.
- (28) Brown, A. M.; Sundararaman, R.; Narang, P.; Goddard, W. A.; Atwater, H. A. *ACS Nano* **2016**, *10*, 957–966, PMID: 26654729.
- (29) Narang, P.; Zhao, L.; Claybrook, S.; Sundararaman, R. *Advanced Optical Materials* **2017**, 1600914–n/a, 1600914.
- (30) Brown, A. M.; Sundararaman, R.; Narang, P.; Goddard, W. A.; Atwater, H. A. *Phys. Rev. B* **2016**, *94*, 075120.
- (31) Brown, A. M.; Sundararaman, R.; Narang, P.; Schwartzberg, A. M.; Goddard III, W. A.; Atwater, H. A. *arXiv preprint arXiv:1608.03309*, upcoming in *Phys. Rev. Lett.* **2016**,
- (32) Rozzi, C. A.; Varsano, D.; Marini, A.; Gross, E. K. U.; Rubio, A. *Phys. Rev. B* **2006**, *73*, 205119.
- (33) Shirodkar, S. N.; Kaxiras, E. *Phys. Rev. B* **2016**, *93*, 245438.
- (34) Guzman, D.; Alyahyaei, H.; Jishi, R. *2D Materials* **2014**, *1*, 021005.
- (35) Roldán, R.; Brey, L. *Physical Review B* **2013**, *88*, 115420.
- (36) Jablan, M.; Buljan, H.; Soljačić, M. *Physical review B* **2009**, *80*, 245435.
- (37) Despoja, V.; Novko, D.; Dekanić, K.; Šunjić, M.; Marušić, L. *Physical Review B* **2013**, *87*, 075447.
- (38) Kinyanjui, M.; Kramberger, C.; Pichler, T.; Meyer, J.; Wachsmuth, P.; Benner, G.; Kaiser, U. *EPL (Europhysics Letters)* **2012**, *97*, 57005.

(39) Low, T.; Guinea, F.; Yan, H.; Xia, F.; Avouris, P. *Phys. Rev. Lett.* **2014**, *112*, 116801.

(40) Profeta, G.; Calandra, M.; Mauri, F. *Nature physics* **2012**, *8*, 131.

(41) Jain, J. K.; Sarma, S. D. *Physical Review B* **1987**, *36*, 5949.